Stochastic magnetic tunnel junction with easy-plane dominant anisotropy

Jonathan Z. Sun ®, Christopher Safranski, Philip Trouilloud, Christopher D'Emic, Pouya Hashemi, and Guohan Hu

IBM T. J. Watson Research Center, Yorktown Heights, New York 10598, USA

We experimentally explore an easy-plane dominant magnetic tunnel junction's thermal stochastic fluctuation for possible applications in physical random number generation for computing. We use materials and fabrication methods similar to those in spin-transfer-torque based magnetic random access memory technology. This work provides an experiment-based view of the device properties that could be optimized for use as an entropy source. We illustrate some relevant device-level metrologies and show several materials and device-physics related factors one could further investigate. Those include the role of a combined strong easy-plane and a weak in-plane anisotropy on fluctuation, the combined stochastic dynamics of the free and reference layer of such magnetic tunnel junctions under bias-voltage induced spin-current drive, and the dynamics' dependence on bias voltage, on magnetic field, and on device and materials parameters in need of control. These observations provide a base-line view of such stochastic tunnel junctions for future applications-specific optimization.

I. INTRODUCTION

For efficient parallel probabilistic computation of optimization problems [1–8], it is desirable to have compact, tunable, power and area efficient physical (true) random number generators (TRNGs). One candidate for such a physical hardware based stochastic signal generating device is a magnetic tunnel junction operating in its free-layer (FL)'s superparamagnetic limit. To mitigate the strong temperature dependence of telegraphing superparamagnetic fluctuations under a uniaxial anisotropy energy potential [9–11], it has been further proposed [12,13] that an easy-plane dominant thin-film nanomagnet operating in small-size limit describable by a macrospin model should possess fluctuation timescales below 1 ns, and be relatively insensitive to temperature, with a $1/\sqrt{T}$ dependence, making it more compatible for state-of-the-art CMOS digital circuit integration as probabilistic bits (p-bits).

Experimentally, an autocorrelation time below 5 ns has been seen in in-plane magnetized stochastic magnetic tunnel junctions [10,14], validating the basic concept of easy-plane dynamics as described by Refs. [12,13]. Many important issues however remain to be clarified, including the identification, and control, of key materials and device-design parameters that govern the easy-plane stochastic magnetic tunnel junction (EP-SMTJ)'s performance and the establishment of practical metrics of such EP-SMTJs for applications, together with the development of related metrology.

Here with these circuit needs in mind, we explore EP-SMTJ devices experimentally to provide a base-line understanding of the issues important to materials and device design and fabrication, issues that can materially impact the EP-SMTJ's fluctuation characteristics. Our approach includes characterizations of (a) the EP-SMTJ's quasistatic resistance-voltage characteristics that can resemble the so-called "sigmoidal" probability bias dependence, (b) the timescale of the EP-SMTJ's fluctuating conductance and its

spin-transfer-torque (STT) bias-voltage dependence, in steady state, and (c) the settling time of the conductance fluctuation distribution as it responds to a stepwise STT bias-voltage change. These results point to the importance of achieving a low level of in-plane anisotropy energy (compared to ambient $k_B T$ where k_B is the Boltzmann constant and T the ambient temperature) for reducing and stabilizing the settling time of the EP-SMTJ's fluctuation distribution.

II. EXPERIMENT

A. Materials and device structure

The EP-SMTJ used in this series of experiments are composed of a synthetic antiferromagnet or SAF-coupled reference layer (RL) underneath a ferromagnetic or SAF-coupled free layer (FL), using materials similar to those developed for spin-transfer-torque based magnetic random access memories (STT-MRAMs) with MTJs [15,16]. Here the relevant film thicknesses are increased to ensure easy-plane anisotropy for all layers.

The EP-SMTJ design here does not include antiferromagnetic pinning for the RL. To have a solid antiferromagnetic exchange pinning, devices would need to be anneal set in field, which for 200 mm MTJ tool-set based processes like ours means a departure from an already optimized route, and requiring additional materials and processing retuning. Moreover, the addition of antiferromagnetic pinning also complicates the thermal (and STT-driven) fluctuation analysis, as the RL cannot be treated as freely rotatable nor simply held at fixed position—one needs to model the antiferromagnetic pinning's thermal fluctuation as well, similar to studies in hard-disk drive read-head noise characteristics. To avoid these complexities, we went with a simpler design without RL pinning.

A representative materials stack is composed of, from substrate up, $\parallel$ 20 TaN $\mid$ 20 Pt $\mid$ 24 $Co_{70}Fe_{30}$ $\mid$ 7 Ru $\mid$ 22 $(CoFe)_{70}B_{30}$ $\mid$ 5 $Co_{70}Fe_{30}$ $\mid$ $\sim$10 MgO $\mid$ 5 $Co_{70}Fe_{30}$ $\mid$
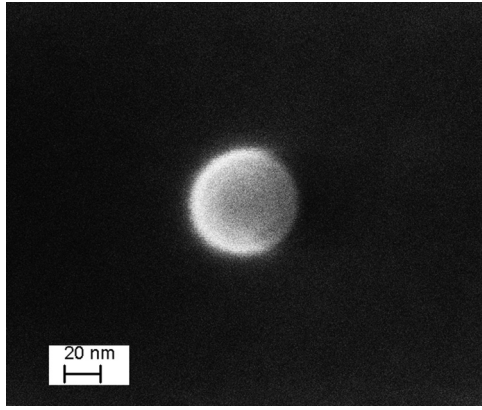
FIG. 1. Planar view SEM micrograph showing the shape of an MTJ post patterning using ion-beam etching process.

25 (CoFe)$_{70}$B$_{30}$ | 50 Ta | 200 Ru ∥. Numbers are film thicknesses in Å. Films are sputter deposited at ambient temperature onto Si/SiO$_2$ wafers, followed by a 300C, 1 h anneal, prior to device fabrication similar to that used for STT-MRAM. The junctions are patterned into circular shaped pillars with bottom and top electrical contacts. The MgO barrier thickness is chosen so that the MTJs have a resistance-area product (RA) around 10 Ω μm^2. Resulting devices with resistances ranging from 5 to 15 kΩ, corresponding to diameters ranging from 29 to 50 nm, are tested for their quasistatic and dynamic transport behaviors.

The deviation of junction shape from a perfect circle could contribute to an in-plane magnetic anisotropy energy, which for our applications is undesirable. For a uniform ferromagnetic disk, the corresponding anisotropy field, if one takes a simple ellipsoid approximation, should be of the order [17]

$$H_k \approx \frac{(4\pi M_s t)}{a(1-\kappa^2)}\{E(A) - K(A) + \kappa[E(B) - K(B)]\}, \quad (1)$$

where M_s is the saturation magnetization of the thin film nanodisk, t is its thickness, a and b are the ellipses' major and minor axes diameters, and $\kappa = b/a < 1$. E and K are elliptic integral functions, $A = 1 - 1/\kappa^2$ and $B = 1 - \kappa^2$.

Junctions used in this study typically have well-defined circular shape, i.e., $\kappa \to 1$. As an example, a scanning electron microscope image is shown in Fig. 1 from a junction pillar prior to top contact build. The figure illustrates the typical quality of "roundness" of the fabricated device.

B. Quasistatic properties

Quasistatic properties here refer to junction transport characterizations with measurement circuit's bandwidth set below 1 kHz. These represent quantities relatable to the >1 ms time-base averaged value of the relevant signal. Here we review our quasistatic junction resistance vs magnetic field behavior and junction's current-voltage characteristics up to bias voltage of the order ±0.6 V. In all quasistatic measurements reported here, the measurement is voltage biased (by a 50 Ω voltage
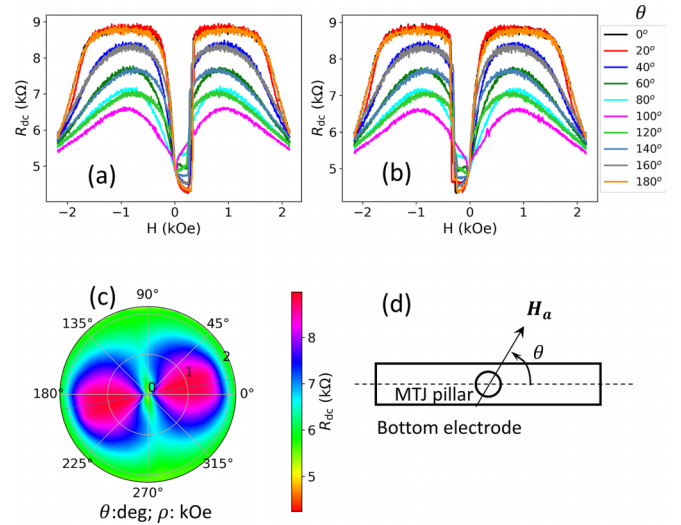

FIG. 2. Example of an EP-SMTJ's quasistatic RH curves at various angles for the applied field. The field is applied in film plane. The bias voltage used is 50 mV. (a) Field sweep from negative to positive direction (up-sweep); (b) down-sweep direction. (c) Polar plot of RH (up- and down-sweep averaged) as a function of field direction, illustrating graphically the presence of an in-plane anisotropy. (d) The definition of applied field angle θ. A low-field RH along $\theta \approx 0$ is given for both samples in Fig. 5 for hysteresis comparison and related device behavior differences.

source) and with junction current sensed on a 100 Ω serial-connected resistor.

1. Resistance-magnetic field behaviors

In this set of our samples, the EP-SMTJ's RLs are not pinned by antiferromagnets and are free to thus also thermally fluctuate or to respond to bias-induced spin torque or to externally applied magnetic fields. A small but noticeable in-plane anisotropy is usually present in resulting device structures. A representative set of quasistatic junction resistance-field (RH) sweep curves is shown in Fig. 2. The magnetic field is applied in the film plane, it is bipolar swept, and then its direction rotated, by 180° in 20° steps, to reveal the in-plane behavior of the EP-SMTJ.

For isotropic in-plane devices one should not expect angular dependence. However, in our devices, an unintended in-plane anisotropy, on the order of a few hundred Oe, is present in most devices, as shown in Fig. 2. The anisotropy varies in magnitude and in direction from device to device and wafer to wafer. This unintended anisotropy is *not* due to imperfection of junction shape. From Eq. (1), to attribute to shape the observed ∼250 Oe in-plane anisotropy, one would have to have $\kappa = b/a \lesssim 0.8$, which is worse than what we have in our shape definition as discussed surrounding Fig. 1. Other possible causes for uncontrolled in-plane anisotropy include film texture related residual crystalline anisotropy and effects from residual in-plane strain through magnetostriction. An estimate based on typical CoFeB magnetostriction values would give an in-plane anisotropy field vs (assuming uniaxial in-plane) strain field relationship of ∼750 Oe/GPa. [18] This highlights the importance of controlling the stress field *within the magnetic layers* for these devices.
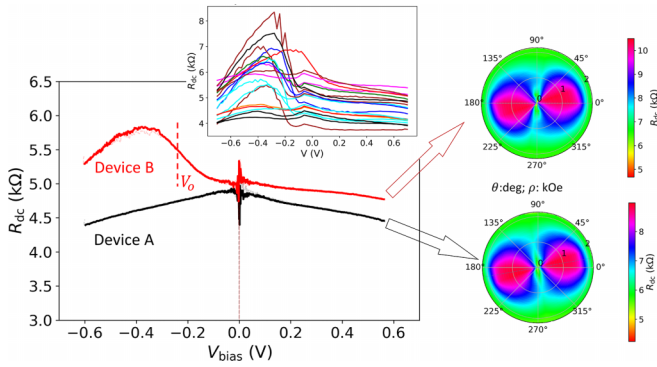
FIG. 3. Example of two EP-SMTJ's RV characteristics: one shows the bias-dependent "sigmoidal-like" tuning characteristic; the other does not. These two junctions have very similar RH and angular dependence characteristics, as shown. Inset: a handful of nominally same junctions, showing a range of variation in their RV sigmoidal characteristics, both in width and in position. All RV are taken with zero applied field. Materials parameters affecting these different behaviors include the SAF RL's exchange coupling strength and the unintended in-plane anisotropies in both RL and FL among others, as discussed below.

2. Resistance-bias voltage dependence

Two types of junction resistance-voltage (RV) behaviors are seen—one type with a bias-voltage dependent resistance change resembling a sigmoidal transition (in addition to the general decrease of high-bias resistance due to inelastic scattering) centering at a certain voltage (V_o, as illustrated in Fig. 3 for device B) and the other without. One pair of junctions illustrating these two types of behaviors is shown in Fig. 3. These two devices have otherwise similar RH angular dependence characteristics. The difference in RV behavior cannot be simply attributed to their difference in unintended in-plane anisotropy alone.

For junctions showing the sigmoidal-like RV characteristics, the center, swing range, and width of the voltage dependence vary from device to device. This is illustrated by a handful of nominally "the same" devices' RV curves in the inset of Fig. 3. The inset RVs come from a different automated screening test on a junction array similar to those in the main panel. They are measured on a coarser voltage step spacing. In all data discussed in this manuscript, junction resistance is defined as $R_{dc} = V_{bias}/I$. Zero offset is removed to avoid singularity in resulting RV plots.

A likely interpretation for this set of behavior shown in Fig. 3 is that it originates from the threshold current for inducing RL1-FL pin-wheel dynamics. Once that gets initiated, the RV tends to a median value between P and AP values and with no strong V dependence of RV over a certain range of spin torque. This particular type of spin-torque dynamics is known in zero-temperature models and in STT-MRAM devices [19–28]. For stochastic MTJ it was also reported in simulations of symmetric two-moment EP-SMTJs by Camsari *et al.* [29]. This mechanism can be sensitive to many materials parameters, including the SAF RL's SAF exchange strength, in addition to the in-plane anisotropies of both FL and RL—both in terms of their absolute strength and their relative values of FL's vs RL's.
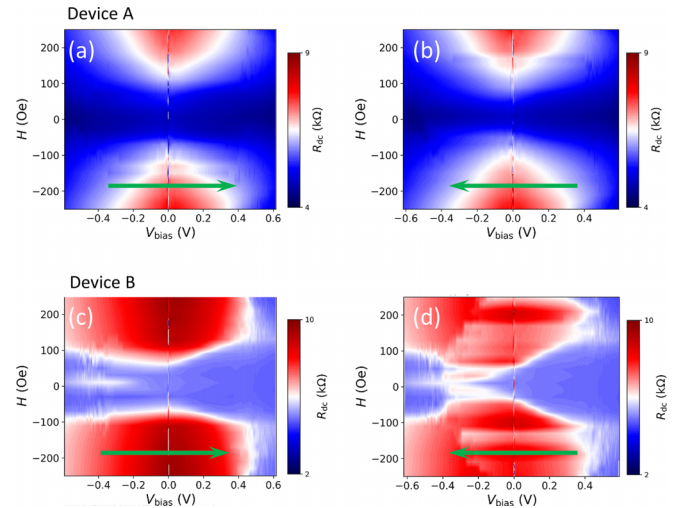

FIG. 4. Bias-voltage and magnetic field dependence of the RV characteristics of the two devices shown in Fig. 2. (a),(b) For "device A." (c),(d) For "device B." Green arrows indicate the direction of voltage sweep.

This point of view is confirmed, albeit indirectly, by measurements from other experimental samples, where the SAF exchange coupling for RL is stronger (with the antiferromagnetic coupling layer in RL reduced from 7 to 3.5 Å of Ru to operate on the first antiferromagnetic RKKY exchange maximum). It turns out that many more junctions in those samples show sigmoidal-like RV than these devices in Fig. 3. This is consistent with a suppression of FL-RL flip-flop dynamics and thus a reduction of junctions showing bias-independent RVs as seen in device A of Fig. 3.

The high voltage bias (up to $\sim \pm 0.6$ V) quasistatic RV behaviors of junctions, at different field-bias values, are shown in Fig. 4, where the RV characteristics upon V sweep are shown as a function of bias magnetic field. The field is applied at 0° angle and is stepped between each successive RV sweep. This shows the sigmoidal-like RV behavior of junctions of nominally the same construct can still vary significantly in $[V_{bias}, H_{bias}]$ space. In the case of device A (with no sigmoidal RV in zero field as in Fig. 3), no voltage-sweep hysteresis is seen. However, for device B, a hysteresis in V sweep is seen in part of the bias field region. These $R[V_{bias}, H_{bias}]$ maps are also dependent on the direction of field applied (not shown). Thus such EP-SMTJ's $R[V_{bias}, H_{bias}]$ is sensitive to materials and device details that need to be optimized for more uniform device-to-device performance.

C. Dynamic stochastic signal with dc bias: "Slow-in, fast-out" measurements

These EP-SMTJ devices are then probed for their high-speed fluctuation characteristics at a given static voltage and magnetic field bias. These are what we call slow-in, fast-out measurements, where the steady-state fluctuation is analyzed in full measurement bandwidth, in our case up to 4 GHz limited by digital oscilloscope (DSP). A comparison of the above defined devices A and B are shown in Fig. 5, which also illustrates the measurement principle.
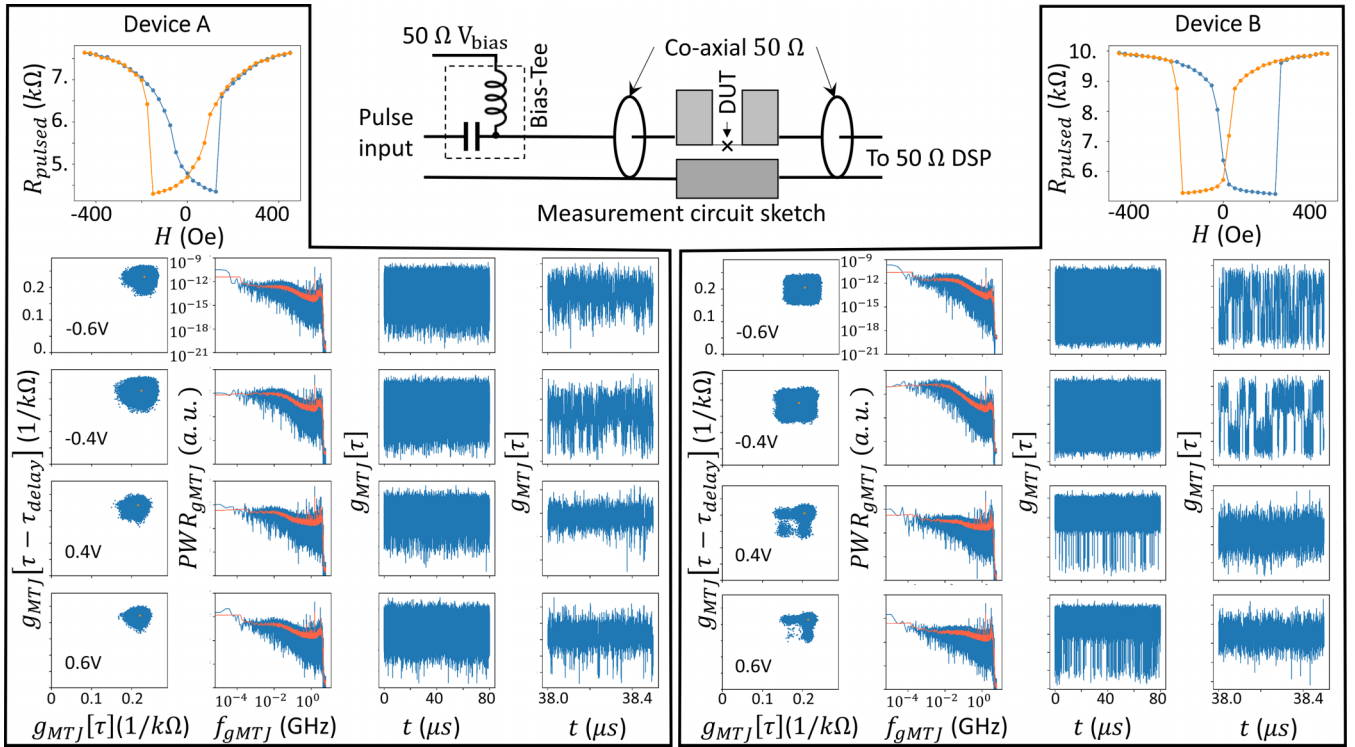
FIG. 5. EP-SMTJ conductance fluctuation at various bias voltage from slow-in, fast-out measurements of devices A and B as defined in Fig. 3. For each device A and B, a pulse-measured (at 200 ns, −0.2 V) device resistance R_{pulse} vs magnetic field, or RH curve, is shown, with field applied along the easy axis as defined in Fig. 3. Below RH are data from slow-in, fast-out measurements, with panels of four columns by four rows. Each row corresponds to one static bias voltage. The first column gives the lag plot of junction conductance in time $g_{MTJ}[\tau - \tau_{delay}]$ vs $g_{MTJ}[\tau]$. $\tau_{delay} = 2.5$ ns. The second column gives the Fourier power spectra corresponding to the full time series. Orange lines are linear scale mean smoothed from blue lines. The third column gives $g_{MTJ}[\tau]$ time traces and the fourth column is the same time trace expanded in timescale. The lag plots of each device have the same y-axes scale. The time-traces data are the same as the lag-plots', but with y axes autoscaled individually for clarity of viewing and scale labels omitted to avoid clutter. The upper-middle inset illustrates the measurement circuit. For slow-in, fast-out measurements, the bias voltage is applied to the dc port of the bias tee. The "pulse input" terminal is where drive pulses are injected in the so-called "fast-in, fast-out" measurements (for R_{pulsed} and other measurements described in sections below).

The device under test (DUT) is measured here with a static dc bias supplied through a bias tee with bias-port cutoff at 80 kHz for 50 Ω loads, as illustrated in Fig. 5's inset. A lag plot [30] illustrates the correlation (or the lack thereof) between junction conductance time dependence and itself at a delayed time by plotting $g_{MTJ}[\tau]$ against $g_{MTJ}[\tau - \tau_{delay}]$. The lag plots in Fig. 5 are delayed by $\tau_{delay} = 2.5$ ns. The values of junction conductance g_{MTJ} here are bounded by the MTJ's parallel and antiparallel state conductance, at the time series' maximum and minimum, plus additional total noise from the measurement circuit. The lag plot of the measurement noise appears as a round cloud resembling a Gaussian distribution and is determined by a combination of Johnson and amplifier noise from the scope. Separate calibration indicates our current measurement noise is $\lesssim 4$ times higher in amplitude than a pure Johnson noise at the corresponding resistive load and bandwidth [31]. Since we are measuring the dynamic current passing through the junction, the resulting measurement noise of junction conductance would depend on the bias voltage, becoming larger in percentage at lower junction bias. This presents a measurement challenge for high-resistance junctions. It can be addressed by using active wideband circuitry at the point of device under test (DUT), which may require

integration of silicon-based active circuitry with the MTJ. This is however outside the scope of this base-line EP-SMTJ study.

The second column for each panel of devices A and B in Fig. 5 shows the Fourier transformed power spectra for the time-dependent junction conductance g_{MTJ}, whose raw time traces are shown at each bias voltage in the third column for full time span (of 80 μs) and in the fourth column for an expanded time span of 0.5 μs, respectively. The high-frequency cutoff in the Fourier power spectra, around 4 GHz, represents the measurement system's bandwidth (cut off primarily by the digitizing scope's bandwidth). A rise at the low frequency end (<10 MHz) of the conductance spectra is seen in almost all data shown, but with somewhat varying magnitude and exact frequency. These reveal the "slower" dynamic features prsent in an EP-SMTJ's superparamagnetic fluctuation.

Now we compare the bias voltage dependence. For both devices, a larger amplitude of conductance fluctuation is seen for negative voltage bias. Note the zero-magnetic field junction resistance, according to their respective RH curves shown in Fig. 5, is close to the low-resistance end, corresponding to an MTJ in its magnetically parallel, or P state, between its FL and RL. In our measurement protocol here, a positive voltage

bias corresponds to a spin-torque attempting to drive the FL of the MTJ towards the direction of the RL (and the same bias would drive the RL moment at the MgO tunnel barrier interface towards the direction *opposite* that of the FL). This is consistent with the observation here in Fig. 5 that a large negative voltage bias results in conductance fluctuations that tend towards the low conductance, or AP state from its more P state at low bias, to the leading order.

For devices A and B, there is a clear difference in the conductance fluctuation's time traces. Compare, for example, data at -0.6 V bias. Device A's lag plot does not have quite the "filling" or squareness as for device B between the P- and AP-state conductance (maximum and minimum conductance). In respective time traces, one could see the difference results from device B's telegraphinglike bistable state fluctuation that is not visible in the data for device A. This difference, a presence of telegraphing states seen in device B and not so prominently in device A, is seen at other bias voltage measured time traces as well. Correspondingly, one also observes a stronger low frequency rise in the conductance spectra for device B where the telegraphing excursion is at its most probable.

These differences are accounted for by the different in-plane anisotropies devices A and B have. Comparing to device B, device A has a broader low-field $R[H]$ transition due to FL mean value change and a lower field magnitude for switching back towards a high-resistance state, a switching related to RL's hysteric reversal. Both are consistent with device A having a lower overall in-plane anisotropy energy compared to that of device B.

As an illustration, for near-zero spin-torque (in low-bias limit) RH cases similar to what is shown in Fig. 5, we calculate a simple Boltzmann distribution mean for $\langle \mathbf{m} \rangle$ of a superparamagnetic nanomagnet with a simultaneous presence of a large easy-plane anisotropy $H_p \gg k_B T/2m$ and a small in-plane easy-axis anisotropy $H_k \ll 8k_B T/m$. This gives an ensemble-averaged moment along the in-plane anisotropy direction (the same direction we call x, where a small external field $H_a \to 0$ is applied) to be

$$\frac{\delta \langle m_x \rangle}{\delta H_a} \approx \frac{m^2}{2k_B T}\left(1 + \frac{mH_k}{8k_B T}\right), \qquad (2)$$

giving an estimate for the "saturation field" H_{sat} defined through $\delta \langle m_x \rangle/\delta H_a \approx m/H_{\text{sat}}$ of

$$H_{\text{sat}} \approx \frac{2k_B T}{m} - \frac{H_k}{4}. \qquad (3)$$

This points to the role of a small, added in-plane uniaxial anisotropy as to *narrow* the m-H transition of thermal fluctuation as described by the saturation field H_{sat}.

An additional consequence of a lower in-plane anisotropy in device A is it can have relatively unstable RL. Under a finite spin-torque bias, such EP-SMTJs are more easily driven into a FL-RL1 pinwheel excitation, causing a correlated fluctuation of its FL and RL, and affecting the tunnel magnetoresistance time dependence, as the tunnel conductance is proportional to the scalar product of FL and RL moment directions: $g_{\text{MTJ}}[\tau] \propto \mathbf{n}_{\text{mFL}} \cdot \mathbf{n}_{\text{mRL1}}$. Here we used $\mathbf{n}_{\text{mRL1}}$ for the EP-SMTJ's first RL layer facing the tunnel barrier, with RL being two layers coupled antiferromagnetically via an
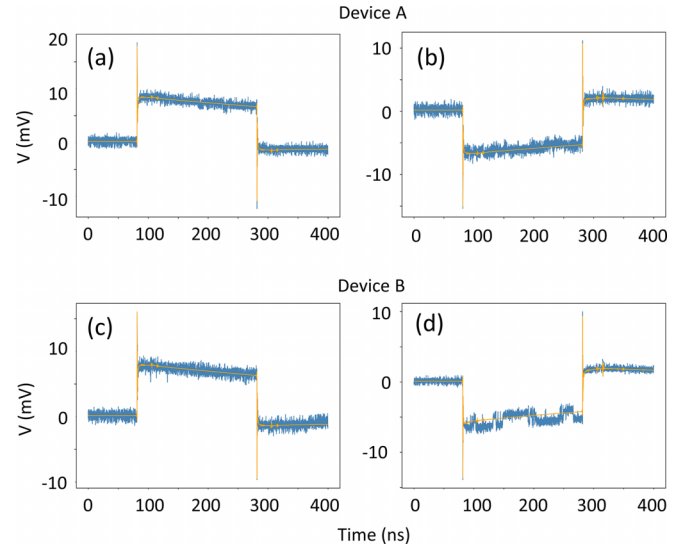

FIG. 6. Sample fast-in, fast-out measurement signals on digitizing scope, for both samples A and B, in two polarities, at ± 0.7 V pulsed voltage. Blue traces are single-trace data. Orange traces are the mean value of 30 000 trace averaged results.

RKKY layer of Ru. In this context, the bias-independent $\langle R \rangle$ shown in Fig. 3 of device A indeed may be a consequence of its being excited at fairly low bias voltages already into this pinwheel motion [29]. This may also affect the different $g_{\text{MTJ}}[\tau]$ characteristics seen for devices A and B as shown in Fig. 5, especially at high bias voltages.

D. Settling time of fluctuation mean value based on stepwise bias voltage driven fast-in, fast-out measurements

Here we examine the "settling time" [32] of these EP-SMTJs' statistical distributions against a stepwise applied spin-transfer torque induced by such a bias-voltage change. For this measurement, a 200 ns wide voltage pulse of various voltages is applied on the pulse input terminal shown in the inset of Fig. 5. The resulting current flowing through the DUT is recorded on the digital scope. One transient trace is recorded together with the averaged trace for each bias voltage. The raw scope traces of two bias voltages at ± 0.7 V are shown in Fig. 6. Blue curves are single-trace recorded data, whereas orange traces are 30 000 trace averaged signals of the same. A sharp spike in the data at the edges of the pulse originates from a parasitic capacitive coupling between the contact pads via a slightly conducting substrate. This parasitic coupling presents another limit to the highest junction resistance one could effectively probe with this method, in addition to noise floor constraints. It does not present a problem for our discussion at present. Also, a slight "drooping" of the otherwise flat top of the 200 ns pulse is seen in these scope signals, which reflects the high-pass frequency characteristics of the bias tee and is not of significant concern for this study for now. It is included in our data analysis shown in Fig. 7 as a linear background with an additional fitting parameter. The noise fluctuations of the blue traces in Fig. 6 represent the combined EP-SMTJ magnetic fluctuation and measurement circuit noise. It is visible in this set of examples that a negatively biased
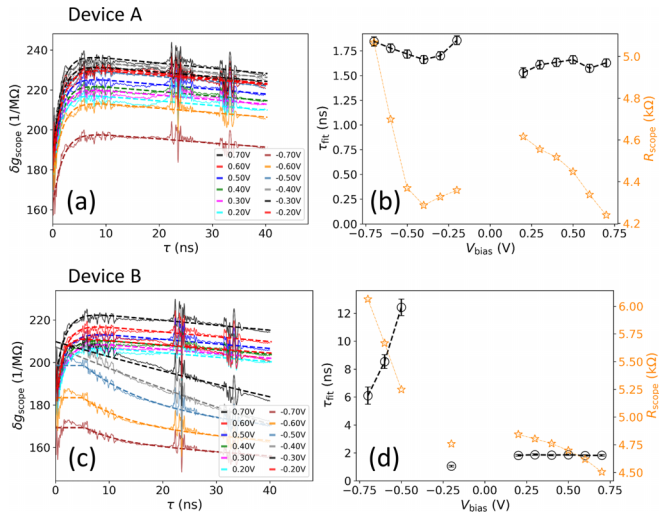
FIG. 7. Analysis of rise-edge time constant of the mean settling as a function of bias pulse height. Panels (a) and (b) are for sample A and (c) and (d) for sample B. Panels (a) and (c) give the bias-pulse height dependent conductance variation. Solid lines are measurement data. Dashed lines fit to a single exponential time-constant function; (b),(d) the corresponding time constant deduced vs bias voltage pulse height. The right-*y* axes (in orange) give the corresponding estimates of the mean junction resistance. The ripples in time-series signals are due to bias-tee related cable reflections.

condition produces more visible "telegraphing" behavior of the signal, as does device B with a higher unintended in-plane anisotropy, all consistent with our discussions surrounding Fig. 5.

We focus on a quantitative analysis of the characteristic timescale of the mean-averaged trace from data such as shown in Fig. 6 and study them as a function of bias voltage that is the pulse height. The resulting time-constant behavior is shown for both samples A and B in Fig. 7.

Data in Fig. 7 point to a bias-voltage dependent settling time (τ_{fit}) for both devices. Device B with a higher unintended in-plane anisotropy as discussed earlier shows a much stronger bias dependence in its settling time, especially for the negative bias region where clear telegraphing dynamics were observed in its steady state as shown in Fig. 5. These results here are only for base-line understanding, as the deduced settling time τ_{fit} is in many cases not significantly longer compared to the measurement cutoff bandwidth. So much so that it is not always possible to distinguish when one is measuring the junction response and when the results are dominated by measurement bandwidth related dynamics. This is especially true for small values of τ_{fit} and also for low bias voltage, where a more significant portion of the fluctuation signal originates from the measurement circuit. However, even with these measurement uncertainties, a clear trend of mean settling time *increase* is seen upon the reduction of magnitude in negative bias voltage. This settling time increase appears more significant for sample B which has more unintended in-plane magnetic anisotropy. These materials properties' dependence needs to be more solidly established, both experimentally and, better yet, theoretically, so as to effectively mitigate its possible impact for applications.

III. DISCUSSIONS

This series of experiments gives a base-line understanding of the factors important for EP-SMTJ, grounded in observations.

First, the unintended in-plane anisotropy needs to be reduced. A rough first-principle based criteria might be for such anisotropies to be below the thermal agitation energy scale $k_B T$ or an effective in-plane anisotropy field (if uniaxial) of $H_k \ll 2 k_B T / m$. This for the device geometries we described above corresponds to a FL in-plane $H_k \ll 35$ Oe, assuming a FL diameter of 35 nm, an effective thickness of 3 nm, and an effective saturation magnetization of the FL as $M_{s,\text{eff}} \approx 800$ emu/cm^3. Such anisotropy fields were not directly measured in this series of experiments, as the RL is not pinned, and its reaction to applied magnetic field interferes with the analysis from RH characteristics. From our data such as in Fig. 3 all we could say is the anisotropy field involved is likely in excess of 200 Oe based on the observed RH shape and hysteresis.

Secondly, a relatively bias independent mean junction conductance is seen in some junctions, while other, nominally identical and practically similar junctions show clear voltage-bias dependent, sigmoidal-like conductance. The behavior of very weak bias voltage dependence of junction RV could originate from the FL-RL coexcitation. This dynamics is observed in our numerical simulations and has also been reported by other group's numerical models [29].

Third, the stochastic dynamics of EP-SMTJ is sensitive to both bias voltage and applied field. Both can affect the fluctuation amplitude (whether full P-AP or otherwise) and temporal characteristics (whether relatively uniform fluctuations over all states between P-AP limit or exhibiting longer dwell time in some preferred directions, causing a telegraphing fluctuation in time series). Since both bias voltage and applied field response of the EP-SMTJ reveal the energy and spin-current scale set by the device materials structure, we will need more direct assessment and control of these materials-related effects. To mitigate or control these behaviors, corresponding device film stack design needs to be optimized, which involves several materials parameters, such as total moment, total easy-plane anisotropy, and total in-plane anisotropy tolerance.

Fourth, the characteristic EP-SMTJ fluctuation distribution's settling time depends both on spin torque (bias voltage in these experiments) and on the anisotropy energy landscape (especially on the presence of in-plane anisotropy). Larger in-plane anisotropy and/or lower bias spin-torque magnitude empirically lead to a longer settling time. This is consistent with the picture of a "double-well" energy landscape bringing in a new timescale involving the hopping rate between the energy minima, with this rate strongly dependent on the energy barrier between the two wells. A high-symmetry (uniaxial only) low barrier limit result is known analytically [9,33]. In our more complex energy landscape, the detailed quantitatives have not yet been fully worked out, but the trend appeared similar, which can be observed with numerical simulation. The impact of such a settling-time variability to various applications needs to be more carefully examined. Regardless, the intrinsic timescale of the EP-SMTJ fluctuation appears to be of the order of a nanosecond, as has been seen in many

of these devices, and in certain instances limited by our test system's bandwidth.

Lastly, we have not directly probed the low-bias limit case of the thermal-fluctuation-only behavior of EP-SMTJ in these experiments. In these experiments, the effect of spin torque has always been intermingled with thermal agitation related dynamics. This is because of the need to probe electrical signals in a 50 Ω environment which requires sizable current flow through the device for any detectable signal. Therefore, while these experiments reveal many important traits of these devices, they have not directly addressed the operation space where a transistor-integrated EP-SMTJ can, and may need

to, perform—in a low spin-torque bias, purely thermal-driven fluctuation regime. This operation space remains to be explored with test vehicles where these EP-SMTJs are integrated with transistor circuit on chip.

[1] K. Y. Camsari, S. Chowdhury, and S. Datta, Phys. Rev. Appl. **12**, 034061 (2019).

[2] K. Y. Camsari, S. Salahuddin, and S. Datta, IEEE Electron Device Lett. **38**, 1767 (2017).

[3] K. Y. Camsari, B. M. Sutton, and S. Datta, Appl. Phys. Rev. **6**, 011305 (2019).

[4] W. A. Borders, A. Z. Pervaiz, S. Fukami, K. Y. Camsari, H. Ohno, and S. Datta, Nature (London) **573**, 390 (2019).

[5] J. Kaiser, R. Faria, K. Y. Camsari, and S. Datta, Front. Comput. Neurosci. **14**, 14 (2020).

[6] A. Z. Pervaiz, L. A. Ghantasala, K. Y. Camsari, and S. Datta, Sci. Rep. **7**, 10994 (2017).

[7] J. Kaiser and S. Datta, Appl. Phys. Lett. **119**, 150503 (2021).

[8] N. A. Adadit, A. Grimaldi, M. Carpentieri, L. Theogarajan, J. M. Martinis, G. Finocchio, and K. Y. Camsari, Nat. Electron. **5**, 460 (2022).

[9] W. F. Brown, Phys. Rev. **130**, 1677 (1963).

[10] K. Hayakawa, S. Kanai, T. Funatsu, J. Igarashi, B. Jinnai, W. A. Borders, H. Ohno, and S. Fukami, Phys. Rev. Lett. **126**, 117202 (2021).

[11] X. Chen, J. Zhang, and J. Xiao, Phys. Rev. Appl. **18**, L021002 (2022).

[12] O. Hassan, R. Faria, K. Y. Camsari, J. Z. Sun, and S. Datta, IEEE Magn. Lett. **10**, 4502805 (2019).

[13] J. Kaiser, A. Rustagi, K. Y. Camsari, J. Z. Sun, S. Datta, and P. Upadhyaya, Phys. Rev. Appl. **12**, 054056 (2019).

[14] C. Safranski, J. Kaiser, P. Trouilloud, P. Hashemi, G. Hu, and J. Z. Sun, Nano Lett. **21**, 2040 (2021).

[15] S. Assefa, J. Nowak, J. Z. Sun, E. O'Sullivan, S. Kanakasabapathy, W. J. Gallagher, Y. Nagamine, K. Tsunekawa, D. D. Djayaprawira, and N. Watanabe, J. Appl. Phys. **102**, 063901 (2007).

[16] D. C. Worledge, G. Hu, D. W. Abraham, J. Z. Sun, P. L. Trouilloud, J. Nowak, S. Brown, M. C. Gaidis, E. J. O'Sullivan, and R. P. Robertazzi, Appl. Phys. Lett. **98**, 022501 (2011).

[17] E. C. Stoner, Philos. Mag. **36**, 803 (1945).

[18] Assuming a bulk magnetostriction coefficient of around $\lambda_s \approx 2 \times 10^{-5}$ [34], which with an $M_s \approx 800$ emu/cm^3 would yield an anisotropy field dependence on strain field of (assuming uniaxial) $\delta H_a / \delta \sigma \approx 750$ Oe/GPa. Thin film CoFeB with Ta

capping likely would have higher magnetostriction values than assumed [35].

[19] Y. B. Bazaliy, D. Olaosebikan, and B. A. Jones, J. Nanosci. Nanoelectron. **8**, 2891 (2008).

[20] Y. B. Bazaliy, arXiv:0710.2564v1.

[21] M. Tsoi, J. Z. Sun, and S. S. P. Parkin, Phys. Rev. Lett. **93**, 036602 (2004).

[22] J. C. Slonczewski, Phys. Rev. B **39**, 6995 (1989).

[23] J. Slonczewski, Theory of spin-polarized current and spin-transfer torque in magnetic multilayers, in *Handbook of Magnetism and Advanced Magnetic Materials*, Spintronics and Magnetoelectronics, edited by H. Kronmüller and S. Parkin (John Wiley & Sons, Ltd., New York, 2007), Vol. 5, p. 2648.

[24] T. Min, J. Z. Sun, R. Beach, D. Tang, and P. Wang, J. Appl. Phys. **105**, 07D126 (2009).

[25] J. Z. Sun, M. C. Gaidis, G. Hu, E. J. O'Sullivan, S. L. B. Nowak, P. L. Trouilloud, and D. C. Worledge, J. Appl. Phys. **105**, 07D109 (2009).

[26] W. Kim, T. D. Lee, and K.-J. Lee, Appl. Phys. Lett. **93**, 232506 (2008).

[27] C. Safranski and J. Z. Sun, Phys. Rev. B **100**, 014435 (2019).

[28] T. Devolder, O. Bultynck, P. Bouquin, V. D. Nguyen, S. Rao, D. Wan, B. Sorée, I. P. Radu, G. S. Kar, and S. Couet, Phys. Rev. B **102**, 184406 (2020).

[29] K. Y. Camsari, M. M. Torunbalci, W. A. Borders, H. Ohno, and S. Fukami, Phys. Rev. Appl. **15**, 044049 (2021).

[30] For definition, see https://www.itl.nist.gov/div898/handbook/eda/section3/lagplot.htm.

[31] Estimate based on zero-bias measured rms scope noise amplitude of around 0.2mV, compared with a Johnson noise at 4GHz bandwidth and a scope impedance of $R_s = 50 \, \Omega$ with the MTJ low-bias resistance load as R_p, giving a Johnson rms on scope as $V_{\text{stotal}} \approx \sqrt{4 k_B T R_s \Delta f (1 + R_s / R_p)} \sim \sqrt{4 k_B T R_s \Delta f}$.

[32] B. C. McGoldrick and J. Z. Sun, IEEE Magn. Lett. **13**, 4506004 (2022).

[33] W. T. Coffey and Y. P. Kalmykov, J. Appl. Phys. **112**, 121301 (2012).

[34] R. C. O'Handley, Phys. Rev. B **18**, 930 (1978).

[35] Y. Fuji, S. Kaji, M. Hara, Y. Higashi, A. Hori, K. Okamoto, T. Nagata, S. Baba, A. Yuzawa, K. Otsu, K. Masunishi, T. Ono, and H. Fukuzawa, Appl. Phys. Lett. **112**, 062405 (2018).